Narrow and Thin Copper Linear Pattern Deposited by Vacuum Cold Spraying and Deposition Behavior Simulation

Kai Ma[1] · Chang-Jiu Li[1] · Cheng-Xin Li[1]

Abstract Compared with ceramic materials, the fabrication of dense metal films requires higher impact velocity in vacuum cold spraying (VCS), also known as aerosol deposition method. In this study, a supersonic nozzle for the fabrication of dense, thin and narrow copper lines was designed. The acceleration behavior of gas and copper particles was investigated through CFD numerical simulation. And the impact behavior of copper particles was studied through finite element analysis. The copper lines with the width of about 200 μm and the height of about 4 μm were directly fabricated on silicon wafers at room temperature without masking. The results show that there is an optimum particle diameter for the impact velocity in particle collision deposition systems. In order to obtain a higher particle impact velocity in VCS, the substrate should be placed behind the high-pressure region of gas shock wave, so that the position of the high-pressure region of the free jet and the position of the bow shock with the substrate coincide as much as possible. Copper particles undergo plastic deformation and particle flattening upon impact and subsequent particle compaction. The width of copper line increased with increasing standoff distance, and maximum height decreased with increasing standoff distance.

Keywords aerosol deposition (AD) · copper · deposition behavior · metal films · vacuum cold spraying (VCS)

✉ Cheng-Xin Li
   licx@xjtu.edu.cn

1 State Key Laboratory for Mechanical Behavior of Materials, School of Materials Science and Engineering, Xi'an Jiaotong University, Xi'an 710049, Shaanxi Province, People's Republic of China

Introduction

With the rapid development of micro-electromechanical systems (MEMS), micro–nano-device manufacturing has attracted more and more attention. Copper, silver and other metals are often used for the electrical and heat dissipating parts of electronic devices because of their excellent electrical and thermal conductivity. Because some circuits are often used in harsh environmental conditions, such as vibration and high temperature, the materials used for conductive and thermally conductive components not only have good electrical and thermal conductivity, but also have high strength and heat resistance. In addition, environmental protection is gaining more and more attention, and it is necessary to find high-efficiency, low-cost and environmentally friendly metallization processes. The traditional methods used to prepare copper thin films include rolling, electroplating (Ref 1), magnetron sputtering (Ref 2) and chemical vapor deposition (Ref 3). It is difficult for the rolling process to prepare metal thin films under 10 microns. Electroplating has serious environmental pollution. Magnetron sputtering and chemical vapor deposition methods are too inefficient to achieve large-scale production, and for the latter, high reaction temperature consumes too much energy. To solve these problems, an environmentally friendly dry metallization process that does not require chemical solutions is needed.

Vacuum cold spraying (VCS), also known as aerosol deposition (AD) method, is a new type of coating preparation process. It can prepare dense or porous ceramics or metal films at room temperature or low temperature by high-speed collision and cumulative deposition of ultra-fine ceramics. As a new type of coating preparation process, it is increasingly used in the preparation of ceramic coatings (Ref 4–9). However, there has not been any in-

depth research in the field of metal coating preparation. Figure 1 shows a schematic diagram of a vacuum cold spraying system. As reported previously (Ref 4, 10), the system is mainly composed of gas source, powder feeder, movable working platform, acceleration nozzle, vacuum chamber, vacuum pump, etc.
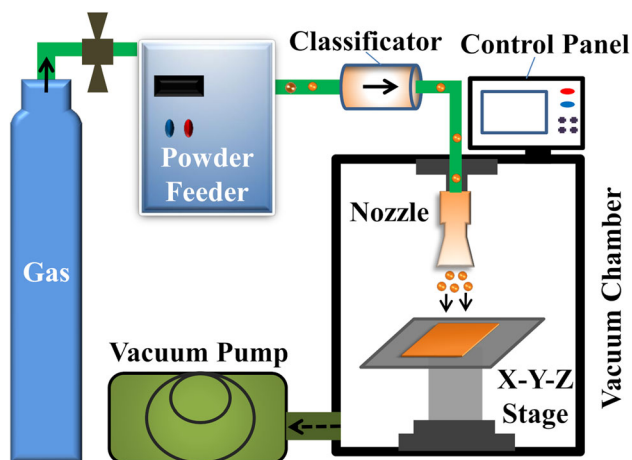
Compared to the low critical velocity of ceramic particles, for example, the critical velocity of alumina is 150 m/ s (Ref 11, 12), the deposition of metals requires a higher impact velocity of hundreds of meters per second (Ref 13). Cold spraying to prepare metal coatings often requires a few megapascals high-pressure gas and several hundred degrees of preheating temperature. In addition, the cold spraying is used by the particle size of dozens of microns. Therefore, it is difficult to prepare thin films less than 20 microns by cold spray (Ref 14). VCS shows the characteristics of depositing small particles, which is essential to obtain thin metal coatings. However, it is necessary to optimize the nozzle for depositing thin metal layers because the deposition behavior of metal is different from ceramic during vacuum cold spraying.

In this research, a simplified Laval nozzle was designed and used. The impact velocities of particles were calculated using computational fluid dynamics (CFD). The impact behavior of copper particles was studied through finite element analysis. The effect of the standoff distance was evaluated. Copper as a typical metal material was used for the deposition of metal and applied to process linear patterns by VCS.

Experiments and Numerical Models

Computational Fluid Dynamics (CFD)

Considering the machinability of the nozzle, the nozzle used in this study is a simplified axisymmetric Laval nozzle, whose geometry is shown in Fig. 2. The main dimensions of the nozzle are listed in Table 1. The diameter of the inlet, throat and exit is chosen as 2, 0.7 and 2.5 mm, respectively. In order to ensure sufficient acceleration of spraying gas flow and particle, the expansion ratio is chosen as 12.8. The convergent part has a length of 10 mm, and the following divergent part has a length of 20 mm. Since the small particles (< 5 μm) adopt local gas velocities quickly, the standoff distance is an important parameter that affects especially the flow field in the deposition process (Ref 15, 16). Hence, the standoff distance varies between 3 and 15 mm.

The CFD code, Fluent (6.2 Fluent Inc.), was used to predict the steady flow field of driving gas as well as the accelerating of particles in VCS. Owing to the axisymmetric characteristic of nozzle used in this study, a 2D axisymmetric model (Ref 16, 17) is shown in Fig. 2. In order to achieve a grid-independent solution, the computational domain was meshed by structured grids with 23,000 nodes. In addition, the grids in the nozzle throat and the region near the wall and substrate were refined. The gas inlet pressure was varied between 0.02 and 0.10 MPa, and the process temperature was kept at 300 K. The gas outlet of the computational domain was treated as pressure outlet with the pressure of 300 Pa. Operating pressure, which is a reference pressure in the software, was set 0 Pa in all simulations. The no-slip condition was invoked at the nozzle wall and substrate surface, and the heat transfer process between the gas and the wall was not considered.

He gas was taken as an ideal and compressible fluid. A coupled implicit method based on the density was used to obtain the flow field. The shear stress transport (SST) RANS model based on the k–ω turbulence model was adopted in the simulation (Ref 15). The SST k–ω model can automatically switch from the wall function to the low Reynolds number formula according to the grid spacing, so as to achieve more accurate near-wall processing (Ref 18).

In this study, copper was used as the spraying particle material. The discrete phase model (DPM) available in Fluent with Lagrangian one-way coupling was used to compute the acceleration of particles inside the VCS nozzle. The heat transfer between the gas and particles had been considered. Duo to low particle volume fraction in the gas phase, particle–particle interactions and the effect of particles on the gas phase can be neglected (Ref 16, 19, 20) and therefore were not accounted for in these simulations. The spherical particles were released uniformly along the inlet boundary of the nozzle with the initial temperature of 300 K. The discrete random walk (DRW) model was applied to predict the particle velocity and distribution. The fundamental fluid dynamic and particle dragging equations used in this model can be found in Reference 21, 22. Five hundred particles were released evenly at the nozzle inlet, and the computing parameters at the substrate were extracted as the corresponding impact parameters.

Fig. 1 Schematic diagram of the vacuum cold spraying system

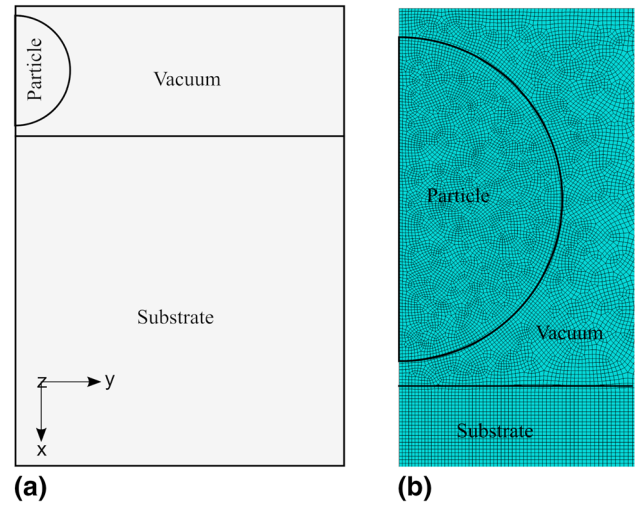**Fig. 2** Schematic diagram of computational domain for fluid dynamic calculations and the boundary conditions
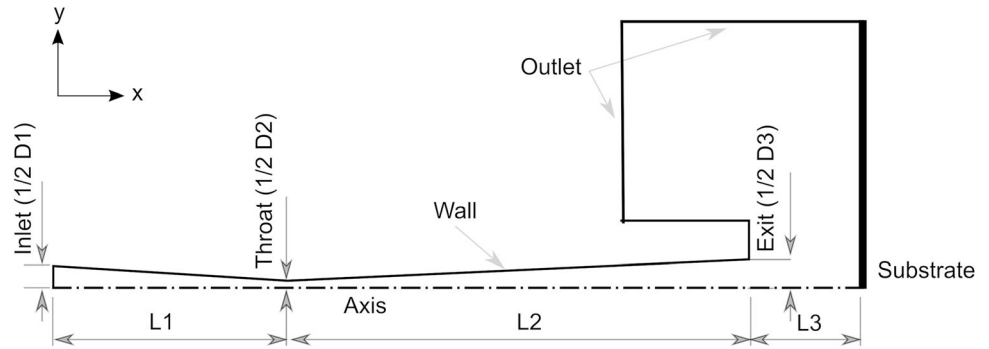
Table 1 Main dimensions of the nozzle used in simulation in this study

Configuration	Dimensions, mm
Inlet diameter, D1	2
Throat diameter, D2	0.7
Exit diameter, D3	2.5
Convergent length, L1	10
Divergent length, L2	20
Standoff distance, L3	3–15

Fig. 3 (a) Symmetric model and computational domain of Cu particle (0.8 μm) impacting on Cu substrate under the Eulerian frame and (b) the enlarged view of elements around the particle with a meshing resolution of 1/100 *d*p

Finite Element Simulation

The explicit finite element analysis software ABAQUS/Explicit was used to simulate the impact behavior of a copper particle using the Eulerian formulation (Ref [23–25]). The heat conduction between the particles and substrates and the heat generation from plastic deformation were considered (Ref [26, 27]). Considering the particle size distribution of the powder used in the experiment, three spherical copper particles with diameters of 0.5, 1.0 and 2.0 μm were used. Since the only available Eulerian element is three-dimensional, a slice with a thickness of 1/20 d_p (where d_p represents the particle diameter) was cut from the middle of the entity model and simplified as a symmetric geometry to reduce the computational cost (Ref [28]), as shown in Fig. 3(a). The meshing was conducted using the 3D Eulerian coupled temperature–displacement 8-node element (EC3D8RT), which considered the heat conduction during the impacting process. The enlarged view of elements around the particle with a meshing is shown in Fig. 3(b), and the meshing resolution was set as $1/100d_p$. The bottom and right boundaries of model were fixed, the left boundary of the model was constrained in the y-direction, and the degrees of freedom in the z-direction were constrained for all elements (Ref [25]).

The material deformation of the particle and substrate was described by the Johnson–Cook plasticity model, which estimates the effects of strain rate hardening, strain hardening and thermal softening. The yield stress (σ_y) of material can be expressed as (Ref [24, 29]):

$$\sigma_y = \left(A + B\varepsilon_{\text{eff}}^{pN}\right)\left(1 + C\ln\dot{\varepsilon}^*\right)\left(1 - \left[\frac{T - T_{\text{room}}}{T_m - T_{\text{room}}}\right]^{*M}\right) \tag{Eq 1}$$

where $\varepsilon_{\text{eff}}^p$ is the effective plastic strain, $\dot{\varepsilon}^*$ is the effective plastic strain rate normalized with respect to a reference strain rate, and T_{room} and T_m are the reference temperature and melting point. A, B, N, C and M are the material-dependent constants for Cu as listed in Table [2] (Ref [25]).

In addition, the elastic behaviors of the particle and substrate were described by a linear Mie–Gruneisen equation of state (EOS). The linear Us–Up Hugoniot formula is defined as (Ref [18]):

$$p = \frac{\rho_0 C_0^2 \eta}{(1 - S\eta)^2}\left(1 - \frac{\Gamma_0}{2}\eta\right) + \Gamma_0\rho_0 E_m \tag{Eq 2}$$

where $\eta = 1 - \rho/\rho_0$ is the nominal volumetric compressive strain, ρ and ρ_0 are the current density and the initial

density, and C_0, S, Γ_0 and E_m, respectively, are the bulk speed of sound, the linear Hugoniot slope coefficient, the material constant named Gruneisen's gamma and the internal energy per unit reference specific volume. The variables C_0, S and Γ_0 used for Cu can also be found in the literature (Ref 25).

The velocities and temperatures of the particles impacting the substrate used in this simulation were predicted using a computational fluid dynamics (CFD) as shown in Table 3. It was assumed that the initial temperature of the substrate was 298 K. The inelastic heat fraction during high-speed deformation was set to 0.9.

Materials and Experimental Details

A commercially available powder copper (ST-M-002-3, St-Nano, China) was used to spray on silicon wafer as substrate. The morphology and the particle size distribution of the starting powder are shown in Fig. 4. It can be observed that the powder exhibits a spherical morphology, and the powder had a d_{50} value of 1.8 μm. For the preparation of copper lines, we used the home-developed vacuum cold spraying (VCS) system by Xi'an Jiaotong University, as shown in Fig. 1. In this study, a redesigned Laval nozzle with a throat diameter of 0.7 mm and the exit diameter of 2.5 mm was used. During spraying, He was used as the accelerating gas and a powder carrier gas. The copper powder was dispersed by the powder feeder and carried out by the carrier gas. Through the acceleration of the accelerating gas in the nozzle, the copper particles collided onto

Table 2 Properties of Cu as spray material and parameters used in impact simulations (Ref 30)

Property	Cu
Density, kg/m^3	8960
Elasticity modulus, GPa	124
Poisson's ratio	0.34
Thermal conductivity, W/(m °C)	386
Specific heat, J/(kg °C)	383
Melting temperature, K	1356
J–C Parameters	
A, MPa	90
B, MPa	292
N	0.31
C	0.025
M	1.09
EOS	
C_0	3940
S	1.49
Γ_0	2.02

the silicon substrate in the deposition chamber. The copper linear patterning was fabricated by controlling the movement of the nozzle in the X–Y plane without masking. The spraying parameters are listed in Table 4 in detail.

Morphologies of feedstock powders and films were examined by field emission scanning electron microscopy (FESEM, MIRA3 LMH, TESCAN, Czech Republic). The samples were broken along the direction perpendicular to the copper line to obtain a cross-sectional sample. The width and thickness of the copper line were measured at the surface and cross section picture, respectively.

Results and Discussion

Results of CFD

In order to verify that the simplified Laval nozzle designed in this study can meet the requirement of spraying copper films, the flow characteristics inside the nozzle and near the substrate were analyzed by numerical simulation. Based on previous research results (Ref 15, 31, 32), several main parameters, including the inlet pressure, standoff distance and diameter of particle were considered. The simulation results also provided data for the adjustment of experimental parameters.

Flow Properties

Figure 5(a), (b) and (c) shows the contour plots of gas speed for three different inlet pressures (P_{in}= 0.02, 0.05 and 0.1 MPa). Gas velocity, pressure and temperature of the flow along the nozzle centerline are plotted in Fig. 5(d), (e) and (f) as functions of distance to the nozzle inlet. For three inlet pressures, the acceleration of the gas velocity inside the nozzle mainly occurs in the throat section where the flow transits from subsonic to supersonic. When gas reaches the divergent part, its velocity keeps increasing continuously when the inlet pressure is greater than 0.05 MPa. However, when the inlet pressure is 0.02 MPa, due to the influence of the boundary layer, the inlet pressure is too small to keep the gas accelerating continuously in the divergent part, so the gas velocity decreases slightly in the divergent part. This can also be confirmed in Fig. 5(d). From Fig. 5(e), it can be found that the gas pressure at nozzle exit, where distance is 30 mm, is higher than ambient pressure (300 Pa); hence, the gas continues with expansion near the exit nozzle. The bow shock with a low-velocity and high-density region always appears near the substrate surface when the supersonic gas jet finally hits the substrate. The gas velocity suddenly reduces from supersonic to zero inside the bow shock. As the inlet pressure increases, the thickness of the bow shock

Table 3 The initial velocity and temperature of particles according to CFD results

Particle diameter, μm	The initial velocity, m/s	The initial temperature, K
0.5	1046	313
1.0	834	233
2.0	552	165

Fig. 4 Morphology of the copper powder (a) and its particle size distribution (b)
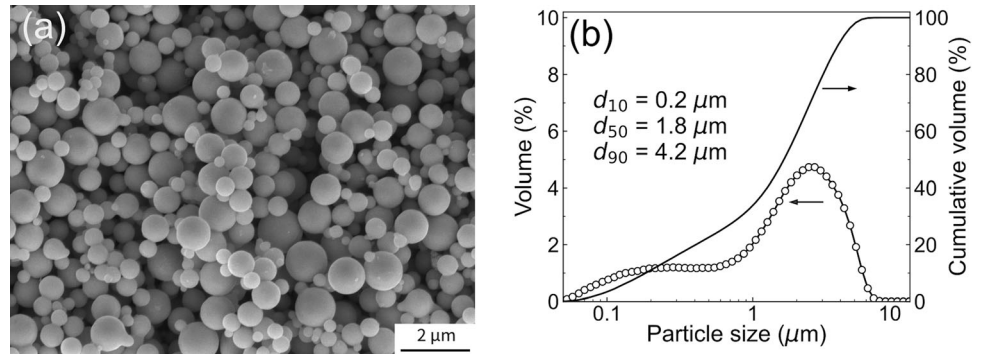
Table 4 Deposition parameters of the vacuum cold spraying experiments

Parameter, Unit	Value
Chamber pressure, KPa	0.3
Pressure in powder unit, KPa	50
Gas flow rate, SLPM	5.5
Distance from nozzle exit to substrate, mm	3–15
Nozzle traversal speed, mm/s	2
Gas temperature, °C	Room temperature

decreases slightly, but the pressure increases significantly. In other words, the gas density in the bow shock increases. The bow shock will prevent particles from passing through, especially for small particles (Ref 33), so increasing the inlet pressure is not conducive to the particles passing through the bow shock. As a result, the gas temperature decreases in the divergent part and increases near the substrate surface in Fig. 5(f). This is because the internal energy of the gas changes to kinetic energy as it expands.

Table 5 shows the summary of calculation results for the three inlet pressures. When the inlet pressure increased from 0.02 to 0.05 MPa, the gas velocity at nozzle exit and maximum gas velocity both increased significantly. Correspondingly, when the inlet pressure increased from 0.05 to 0.1 MPa, the gas velocity at nozzle exit and maximum gas velocity increased slightly. As the inlet pressure increased, the gas temperature at nozzle exit increased, while the gas temperature at nozzle exit decreased. In addition, the gas flow also increased as the inlet pressure increased. When the inlet pressure increased from 0.02 to 0.10 MPa, the Cu particle impact velocity only slightly

increases. Hence, taking into account the cost of gas consumption and synthesizing the above calculation results, it is sufficient to select an inlet pressure of 0.05 MPa for deposition experiments.

Particle Acceleration

Figure 6 shows the simulation results of copper particles with particle size between 0.1 and 5.0 μm. The velocity of the gas flow and the particle paths along the nozzle centerline are shown in Fig. 6(a). The movement of the particles can be divided into two stages: In the first stage, the particles are dragged and accelerated by the carrier gas inside the nozzle. In the second stage, due to the presence of bow shock near the substrate, the particles experience a speed drop or deflection, and not all particles can hit the substrate. For small particles (less than 0.3 μm), because of the smaller inertia of particles, they are easier to accelerate with the gas in the nozzle, but they also are more affected by the bow shock near the substrate and respective deceleration. Especially for the particles with a diameter less than 0.1 μm, the particle's direction are completely deflected and finally move along the streamline to leave the simulation area [shown by the yellow line in Fig. 6(b)]. This result can correspond to previous reports (Ref 32, 34, 35). For large particles (larger than 1 μm), due to the larger inertia of the particles, they are difficult to accelerate with the gas, but they are easier to pass through the bow shock to hit the substrate [shown by the red line in Fig. 6(b)].

Figure 6(c) shows the maximum particle velocity (V_{max}) during the particle paths and the corresponding particle velocity upon impact (V_{impact}) for different particle diameters. The particle maximum velocity decreases with
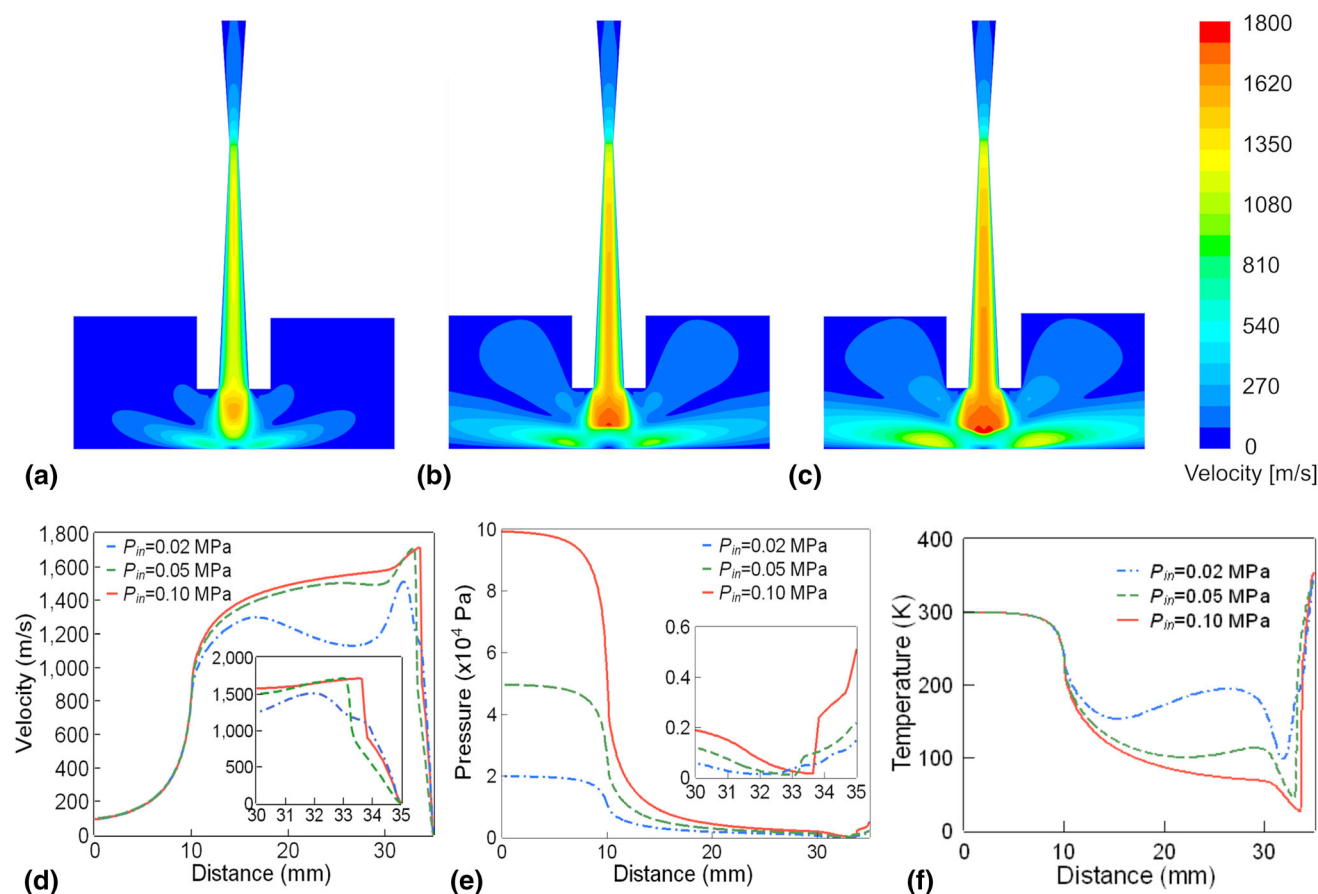
Fig. 5 CFD gas flow velocity results when P_{in} = 0.02 MPa (a) 0.05 MPa (b) and 0.10 MPa (c), and changes in velocity (d), pressure (e) and temperature (f) of flow along the nozzle centerline with three difficult P_{in}

**Table 5** Summary of gas flow simulation results

Inlet pressure, MPa,	Velocity at exit center, m/s	Maximum velocity, m/s	Pressure at exit center, Pa	Temperature at exit center, K	Gas flow, SLPM	1 μm Cu particle impact velocity, m/s
0.02	1253	1511	569	165.7	1.98	814
0.05	1503	1716	1216	110.5	5.50	834
0.10	1579	1717	1899	67.5	11.48	844

particle diameter, but the particle impact velocity initially increases with particle diameter and then decreases with it, with a maximum impact velocity for 0.5-μm-diameter particles. For this model, the maximum particle impact velocity with a particle diameter of 0.5 μm reaches 1088 m/s accordingly. As particles traverse through the nozzle, they are first accelerated by the carrier gas and then decelerated by bow shock region near substrate surface. Hence, the particle impact velocity is the integrated result of the acceleration process and the deceleration process. In addition, the particle size impacting at the highest velocity

can be adjusted by adjusting the inlet gas pressure and vacuum chamber pressures.

In addition, as shown in Fig. 6(d), due to the conservation of energy, the gas velocity increased, but the gas temperature decreased in the nozzle, and the particle temperature will also decrease during acceleration correspondingly. Afterward, the particle temperature increased with the increase in the gas temperature near the substrate. But since this process occurred in a short time, the temperature of the small particles is more likely to increase. This caused the particle temperature upon impact to decrease as the particle diameter increased. Lower particle

Fig. 6 Simulation results of copper particles acceleration: (a) Velocity of gas flow and particle paths along the nozzle centerline. (b) Contour plots of flow velocity near the substrate. (c) Maximum velocity and impact velocity of particle as a function of sizes at the nozzle centerline. (d) Maximum temperature and impact temperature of particle as a function of sizes at the nozzle centerline
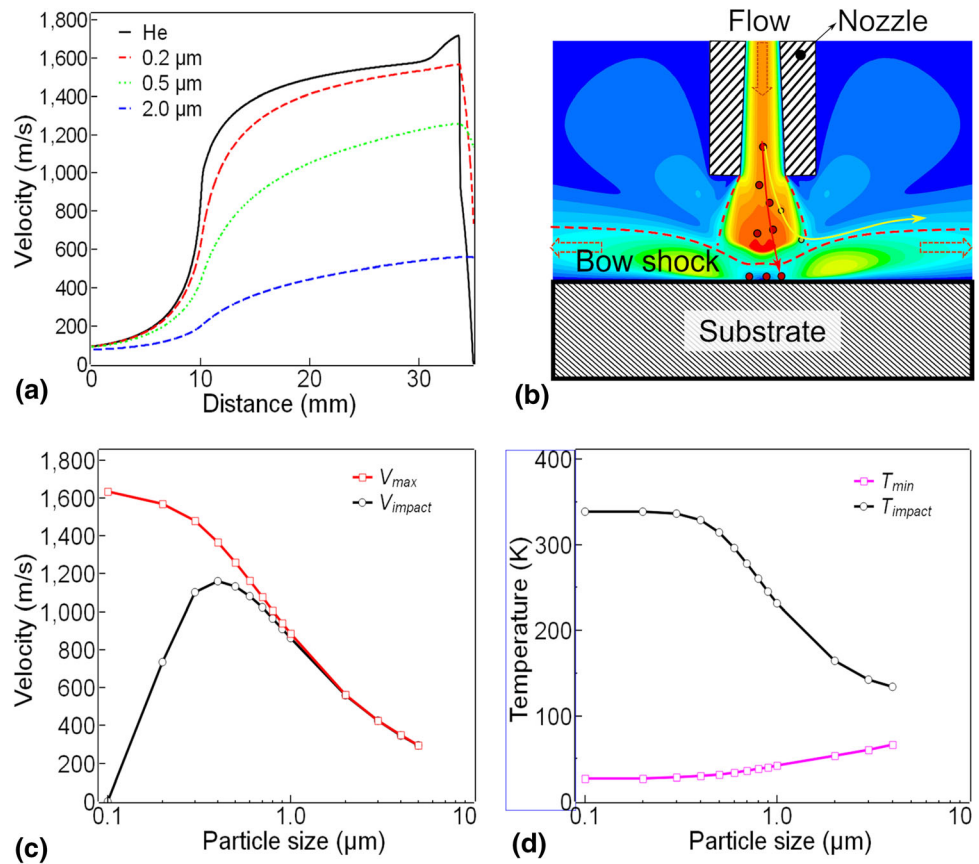
temperature upon impact is not conducive to reducing the critical velocity and subsequent coating formation (Ref 14, 36).

As another important parameter, the standoff distance also has an effect on the particle impact speed and then on the coating deposition efficiency. Figure 7 shows the simulation results of the effect of standoff distance on the flow field and particle velocity. From contour plots of flow velocity at SoD = 3, 5, 9 and 15 mm shown in Fig. 7(a), (b), (c) and (d), it can be observed that the standoff distance does not affect the distribution of flow field inside the nozzle; it only affects the formation of shock waves after the nozzle exit and the bow shock near the substrate. It can also be confirmed in Fig. 7(e) and (f), which shows the gas velocity and gas pressure along the nozzle centerline from the nozzle exit to the substrate. As the standoff distance increases, there is enough distance for the formation of shock waves after nozzle exit. Also, the thickness of the bow shock increases, but the pressure in the bow shock area shows a fluctuation change with standoff distance. Figure 7(g) shows the particle impact velocity with different particle diameters at a standoff distance between 3 and 15 mm. Small particles ($d_p<$ 0.5 μm) exhibit a

fluctuating impact velocity with increasing standoff distance, while the particle impact velocity for larger particles ($d_p>$ 1.0 μm) increases slightly with standoff distance. This is because, as the distance increases, the particles will continue to be accelerated, but the change in the thickness and internal pressure of the bow shock seriously affects the passage of particles, particularly that of small ones. The thickness and internal pressure of the bow shock determine the deceleration rate of the particles. There are a large number of small particles ($<$ 0.5 μm) in the powder used in vacuum cold spraying. Hence, in order to obtain a higher particles impact velocity, the substrate should be placed behind the high-pressure region, so that the position of the high-pressure region of the free jet and the position of the bow shock with the substrate coincide as much as possible, instead of the lowest pressure location mentioned in the literature (Ref 33).

The particle impact velocity as functions of impact position at standoff distances between 3 and 15 mm is shown in Fig. 7(h). The impact positions of large particles are more concentrated near the centerline of the nozzle. On the contrary, the small particles are more widely distributed on the substrate. The impact position range of all particles
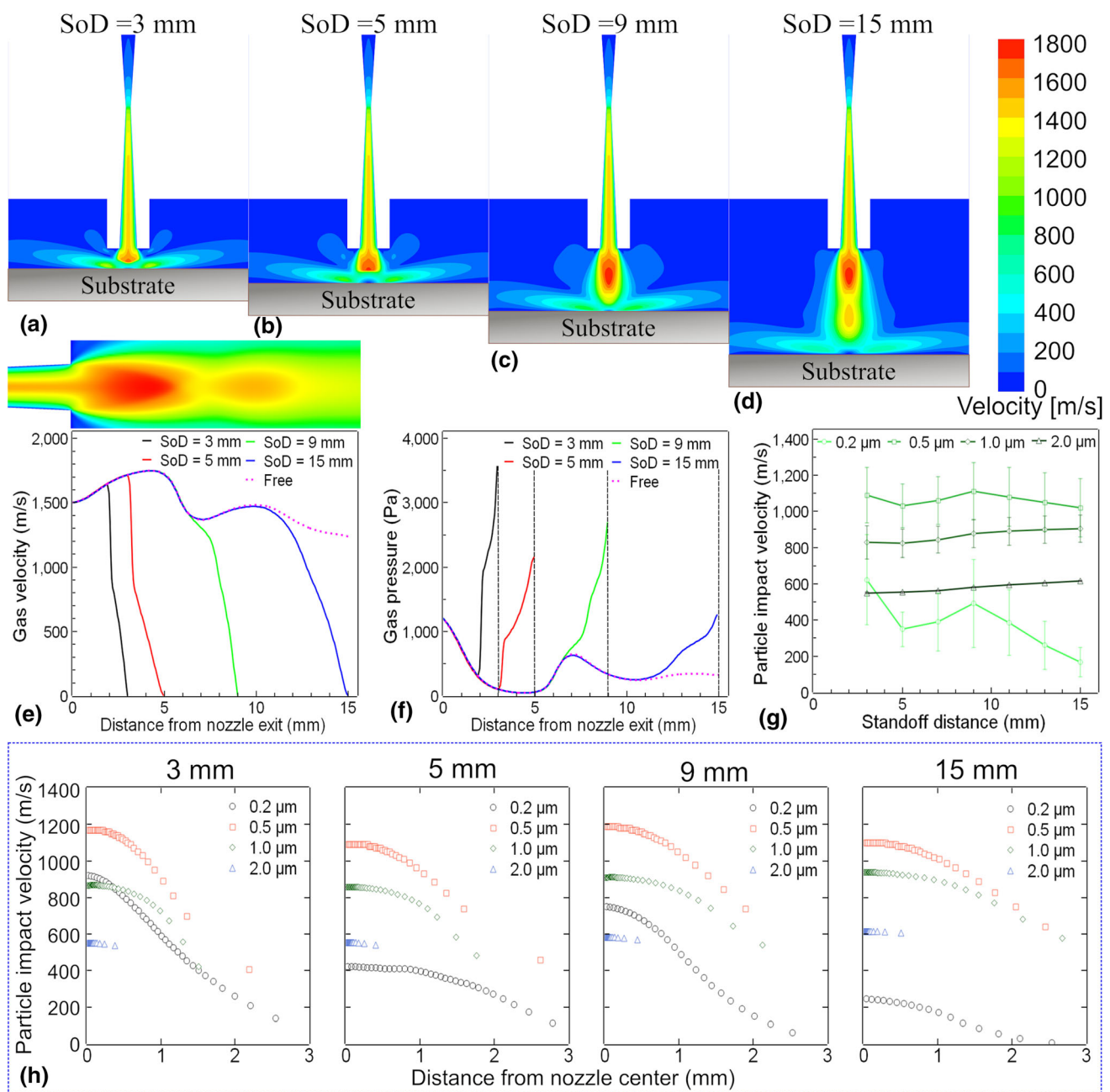
Fig. 7 Contour plots of gas flow velocity at (a) *SoD* = 3 mm, (b) 5 mm, (c) 9 mm and (d) 15 mm. (e) Gas velocity and (f) gas pressure along the nozzle centerline from nozzle exit to substrate. (g) Particle impact velocity for different particle diameters at standoff distances of 3 to 15 mm. (h) Particle impact velocity and impact position at standoff distances of 3–15 mm

will widen as standoff distance increased, which is consistent with the trend of experimental results reported in the literature (Ref 16).

Modeling Results on Cu Particle Impacting on Cu Substrate

It is well known that the particle impact velocity and temperature are important factors for particle deposition,

and many experimental observations also show that particle deformation is a strong function of particle impact velocity (Ref 28, 37). The particles must be accelerated to a sufficiently high speed to successfully deposit on the substrate. Figure 8 shows the simulation results of copper particle deposition for three diameter particles (0.5, 1.0 and 2.0 μm), whose initial velocity and temperature are listed in Table 3 calculated by CFD. Figure 8(a), (b) and (c) shows the simulated contours of equivalent plastic

strain (PEEQ, left side) and temperature (TEMP, right side) of the three particles. All particles are severely deformed, forming a jet composed of both the particles and substrate materials at the particle/substrate interface. The particles

flattened to form a lens-like shape. The velocity corresponding to the initial formation of a jet during the impact process can be considered as the critical velocity of deposition (Ref 28). It can be observed that the largest

Fig. 8 Simulation results of Cu particle impacting on Cu: equivalent plastic strain (PEEQ, left side) and temperature (TEMP, right side) for the particle with diameters of (a) 0.5 μm, (b) 1.0 μm and (c) 2.0 μm, evolution of (d) maximum PEEQ and (e) maximum temperature of the area near the interface between Cu particle and the Cu substrate
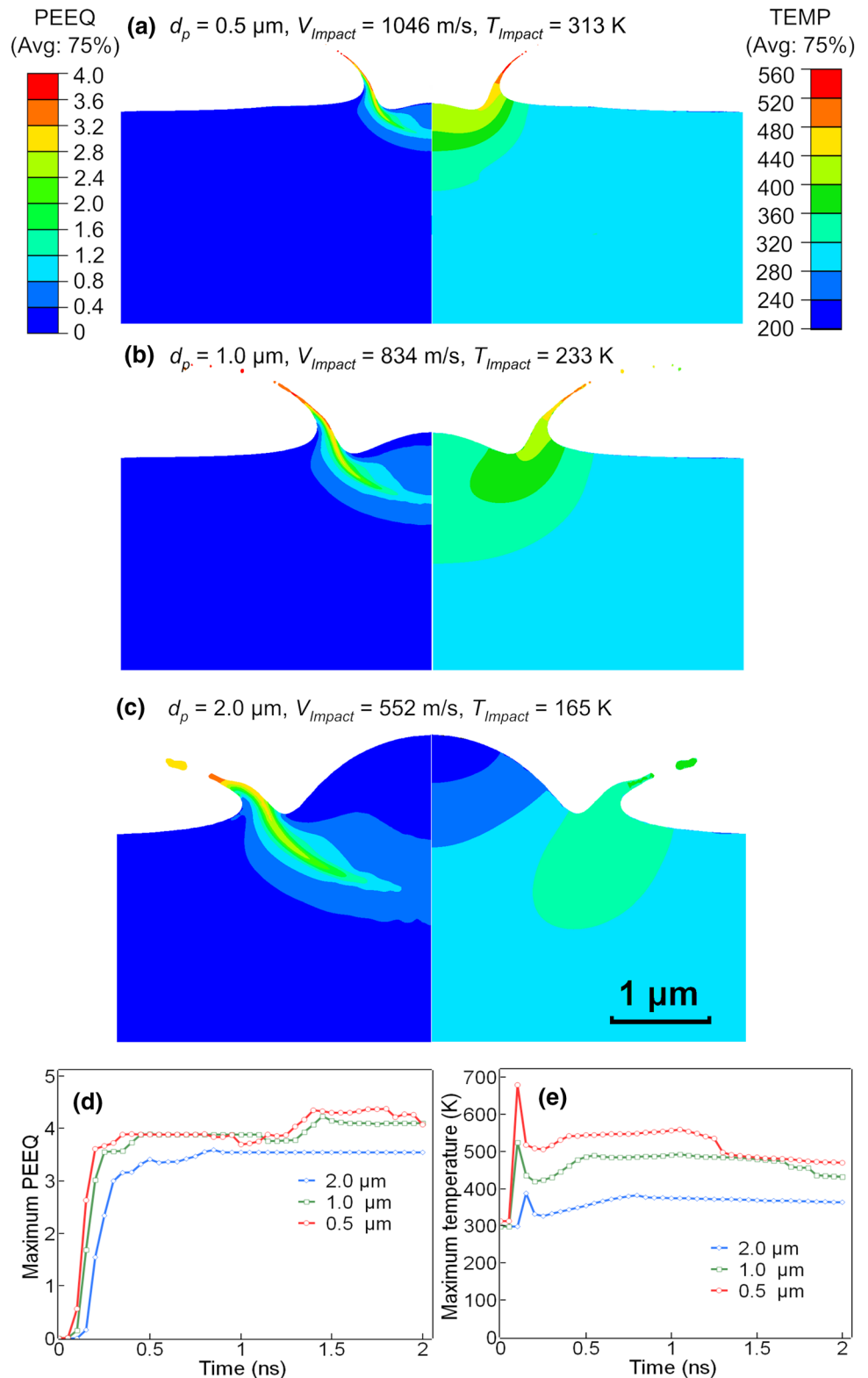
PEEQ is concentrated around the contact zone, and the largest temperature zone is concentrated near the jet, rather than in the center of the initial impact point. Due to the lower velocity of the particle with a diameter of 2.0 µm, the depth-to-width ratio of the crater on the substrate is the smallest, which is 0.22, and the jet just forms at the interface. Correspondingly, for the particle with a diameter of 0.5 µm, the high impact velocity caused the largest depth-to-width ratio of the crater, up to 0.35, and obvious jet forms at the interface. For 1.0-µm particle, the result is somewhere in between.

Figure 8(d) and (e) shows the evolution of maximum PEEQ and maximum temperature of the area near the interface between Cu particle and the Cu substrate with the impact time for three diameter particles. It can be seen that the maximum PEEQ and maximum temperature increase with the impact time in the early impact process, and subsequently they reached a steady state for all particles. It is consistent with the literature (Ref 28); adiabatic shear instability (ASI) cannot be clearly detected just by the steep change in temperature and plastic strain evolution. In short, the simulation results show that the simplified Laval nozzle in this study can meet the requirements of copper particle deposition.

Microstructures of Copper Linear Pattern

After the numerical simulation of the flow field distribution and particle acceleration, as well as the analysis of the deposition behavior through finite element simulation, the copper lines were successfully prepared on the silicon wafer by using the parameters listed in Table 4 via VCS using different standoff distances between 3 and 15 mm. Figure 9(a) and (b) shows a surface SEM micrograph of Si substrate partially covered by Cu and a Cu film. Three particle morphologies can be observed: (1) the copper particles that directly impact on the silicon wafer substrate are completely flattened and form a jet at the edge, corresponding to the blue arrows in Fig. 9(a). (2) The copper particles that hit the first layer of copper particles deposited previously are embedded into those deposited previously, would be less flattened, corresponding to the red arrows in Fig. 9(a). (3) The copper particles on the surface of the copper film are embedded in the previously deposited copper particles and create a jet at the interface, corresponding to the green arrows in Fig. 9(b). Most particle morphologies correspond well to the simulation results in "Modelling Results on Cu Particle Impacting on Cu Substrate" section. The results of the experiment are consistent with the results of the simulation; thus, it is possible to use numerical simulation to predict experimental results and guide experimental parameter in VCS. Figure 9(c) and (d) shows the cross-sectional SEM micrograph of Cu film

with and without polishing. The deformation and flattening of the particles can be observed, which is caused by particle impact deformation and subsequent particle tamping. In addition, the particle interface can be observed, which may be caused by the existence of an oxide film on the surface of the particle (Ref 38).

A schematic diagram of the copper particle deposition process is shown in Fig. 9(e). The deposition process of copper particles on the silicon substrate can be divided into three stages: First, the copper particles hit the silicon wafer substrate. Since the silicon wafer cannot undergo cooperation plastic deformation with copper particles, the copper particles are completely transformed into flakes. The copper particles subsequently impinging on the copper particles deposited previously are embedded in the deposited particles, but some flattening will occur due to the influence of the substrate. Finally, as the thickness of the copper film increases, the subsequent particle deposition is no longer affected by the substrate, and the copper film and the copper particles can deform cooperatively, resulting in a morphology consistent with simulation results shown in Fig. 8(a), (b) and (c). In addition, particle impact subsequently has a tamping effect on the deposited particles to help to close porosity in the film, which is the same process as the cold spray metal coating (Ref 39).

Copper lines were prepared with different standoff distances by VCS. The results of the maximum height and the width of copper lines are shown in Fig. 10. It can be found that the copper lines with a width of about 200 µm and a height of 4 µm can be directly fabricated on the silicon wafer by VCS without masking. The width of copper lines increases, and the maximum height decreases with increasing standoff distance. Since a diverging geometry of Laval nozzle was used in these spray experiments, the deposition area should increase with increasing standoff distance. A similar trend is found with cold spraying results (Ref 16). However, due to the existence of shock diamonds near Laval nozzle exit, the height and the width of copper lines are not linearly related to the standoff distance, which is also discussed in "Particle Acceleration" section.

By setting the scanning track, various copper linear patterns were prepared on a silicon wafer as shown in Fig. 11. Copper linear pattern and copper film can be prepared directly by VCS. In summary, VCS technology can be used not only for the preparation of ceramic films, but also for the applications of dense metal films for surface metallization of nonmetallic materials. Moreover, the bonding mechanism between the copper film and silicon substrate and the control of oxygen content in the copper film still need further study.

Fig. 9 Experimental results when the standoff distance is 3 mm: Surface SEM micrograph of (a) Si substrate partially covered by Cu and (b) Cu film (the blue arrows: the particles that directly impacted on the silicon wafer substrate, the red arrows: the particles that impacted the first layer of copper particles deposited previously, the green arrows: the particles that impacted the copper films deposited previously), Cross-sectional SEM micrograph of Cu film (c) without and (d) with polishing (the red dashed line indicates the outline of the deposited particles), (e) schematic diagram of copper particle deposition process (Color figure online)
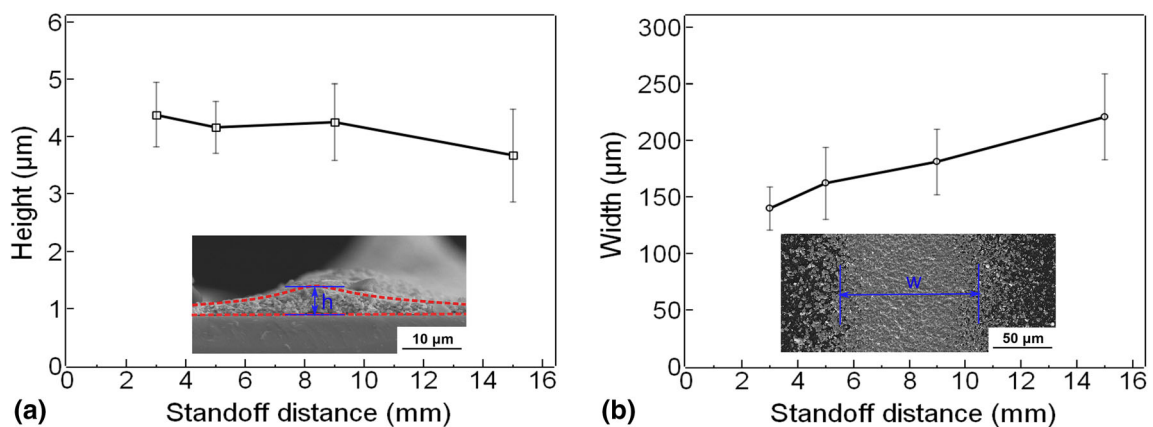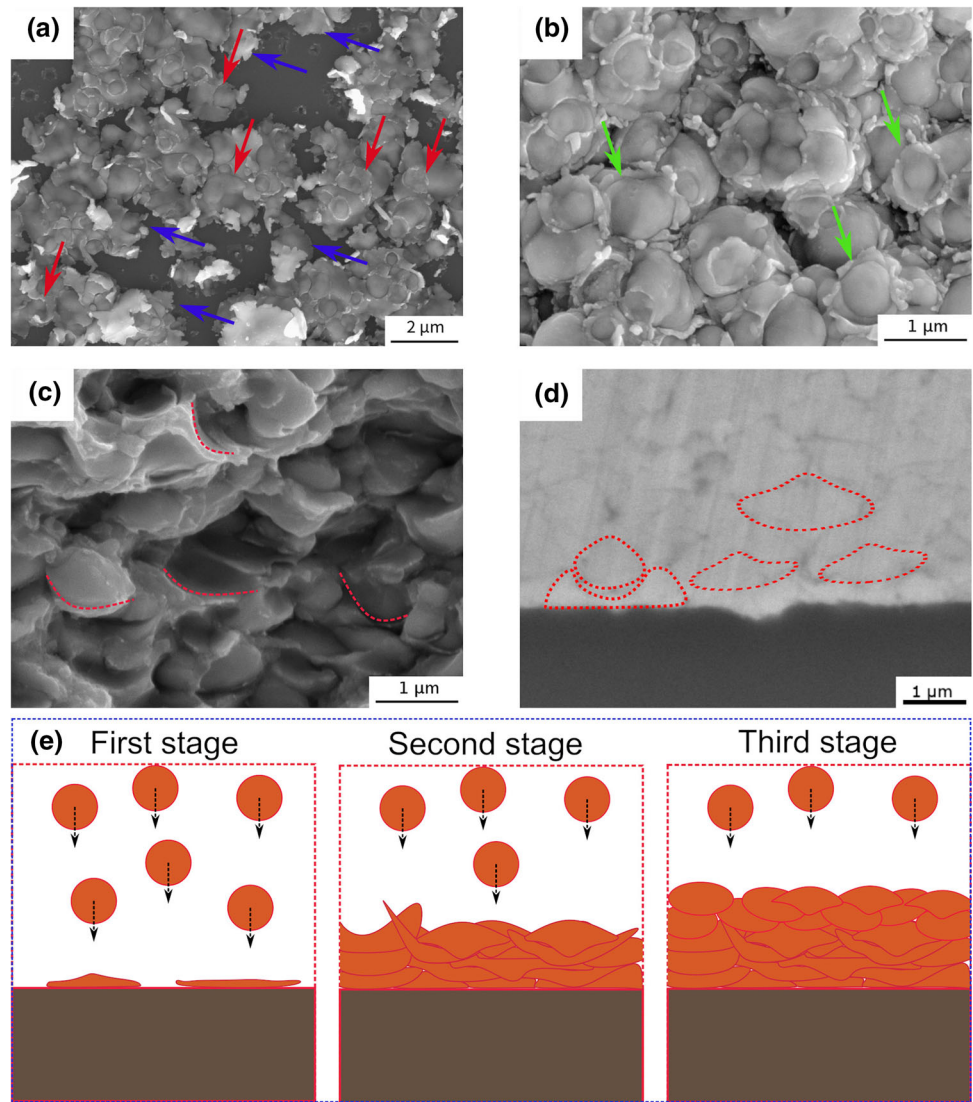
Fig. 10 (a) Maximum height and (b) width of copper lines according to standoff distance

Fig. 11 Copper linear pattern on silicon prepared by VCS: (a) "XJTU" and (b) fringe pattern
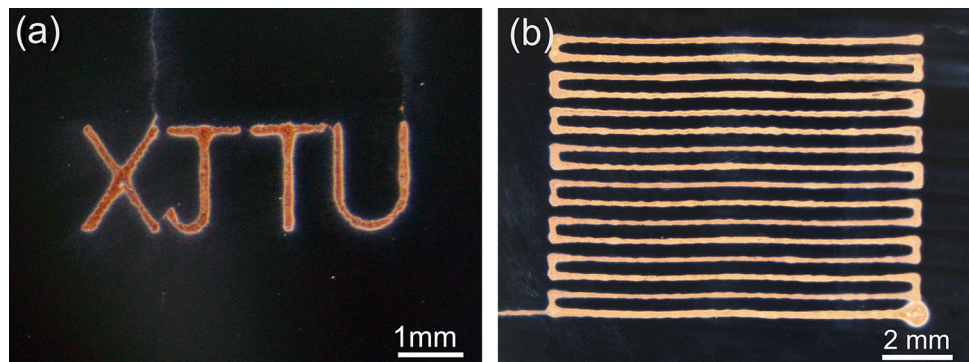
Conclusions

A supersonic nozzle for the fabrication of dense, thin and narrow copper lines was designed. CFD simulation results show that the bow shock with a low-velocity and high-density region always appears near the substrate surface. As the inlet pressure increases, the thickness of the bow shock decreases slightly, but the pressure increases significantly. Meanwhile, the gas velocity increases and the gas temperature decreases. However, the Cu particle impact velocity only slightly increases. The particle impact velocity is the integrated result of the acceleration process along with carrier gas in the nozzle and the deceleration process in the bow shock before impacting. Hence, there is an optimum particle diameter for the impact velocity in a collision deposition system. Because shock diamonds mainly affect the thickness and pressure (density) of the bow shock under different standoff distances, the bow shock affects the particle impact velocity. In order to obtain a higher particle impact velocity in VCS, the substrate should be placed behind the high-pressure region of gas shock wave, so that the position of the high-pressure region of the free jet and the position of the bow shock with the substrate coincide as much as possible.

The copper lines with a width of 200 μm and a height of 4 μm were directly fabricated on the silicon wafer at room temperature by VCS without masking. The deposition process of copper particles on the silicon substrate can be divided into three stages: Particles hit the wafer, particles hit the deposited copper particles close to the substrate, and particles hit the deposited copper particles far from the substrate. The width of copper lines increase with increasing standoff distance, and maximum height decreased with increasing standoff distance. In a word, VCS can be used not only to prepare ceramic films, but also to prepare metal films.

References

1. K.M. Takahashi, Electroplating Copper onto Resistive Barrier Films, *J. Electrochem. Soc.*, 2000, **147**(4), p 1414

2. J.F. Pierson, D. Wiederkehr, and A. Billard, Reactive Magnetron Sputtering of Copper, Silver, and Gold, *Thin Solid Films*, 2005, **478**(1–2), p 196-205

3. J.A.T. Norman, B.A. Muratore, and P.N. Dyer, A New Metal-Organic Chemical Vapor Deposition Process for Selective Copper Metallization, *Mater. Sci. Eng., B*, 1993, https://doi.org/10.1016/0921-5107(93)90085-2

4. J. Li, Y. Zhang, K. Ma, X.-D. Pan, C.-X. Li, G.-J. Yang, and C.-J. Li, Microstructure and Transparent Super-Hydrophobic Performance of Vacuum Cold-Sprayed Al2O3 and SiO2 Aerogel Composite Coating, *J. Therm. Spray Technol.*, 2018, **27**(3), p 471-482

5. L.-S. Wang, C.-X. Li, K. Ma, S.-L. Zhang, G.-J. Yang, and C.-J. Li, La0.8Sr0.2Ga0.8Mg0.2O3 Electrolytes Prepared by Vacuum Cold Spray under Heated Gas for Improved Performance of SOFCs, *Ceram. Int.*, 2018, **44**(12), p 13773-13781

6. L.-S. Wang, C.-X. Li, K. Ma, S.-L. Zhang, G.-J. Yang, and C.-J. Li, Microstructure and Electrochemical Properties of La0.8Sr0.2Ga0.8Mg0.2O3 Thin Film Deposited by Vacuum Cold Spray for Solid Oxide Fuel Cells, *ECS Trans.*, 2017, **78**(1), p 405-412

7. S.Q. Fan, G.J. Yang, C.J. Li, G.J. Liu, C.X. Li, and L.Z. Zhang, Characterization of Microstructure of Nano-TiO2 Coating Deposited by Vacuum Cold Spraying, *Proc. Int. Therm. Spray Conf.*, 2006, **15**(4), p 513-517

8. Y. Liu, Y.Y. Wang, G.J. Yang, J.J. Feng, and K. Kusumoto, Effect of Nano-Sized TiN Additions on the Electrical Properties of Vacuum Cold Sprayed SiC Coatings, *J. Therm. Spray Technol.*, 2010, **19**(6), p 1238-1243

9. L.S. Wang, H.F. Zhou, K.J. Zhang, Y.Y. Wang, C.X. Li, X.T. Luo, G.J. Yang, and C.J. Li, Effect of the Powder Particle Structure and Substrate Hardness during Vacuum Cold Spraying of Al2O3, *Ceram. Int.*, 2017, **43**(5), p 4390-4398

10. S.-Q. Fan, C.-J. Li, C.-X. Li, G.-J. Liu, G.-J. Yang, and L.-Z. Zhang, Preliminary Study of Performance of Dye-Sensitized Solar Cell of Nano-TiO2 Coating Deposited by Vacuum Cold Spraying, *Mater. Trans.*, 2006, **47**(7), p 1703-1709

11. J. Akedo, Aerosol Deposition of Ceramic Thick Films at Room Temperature: Densification Mechanism of Ceramic Layers, *J. Am. Ceram. Soc.*, 2006, **89**(6), p 1834-1839

12. H. Park, H. Kwon, and C. Lee, Inflight Particle Behavior in the Vacuum Kinetic Spray Process, *J. Therm. Spray Technol.*, 2017, **26**(7), p 1616-1631

13. F. Gärtner, T. Stoltenhoff, T. Schmidt, and H. Kreye, The Cold Spray Process and Its Potential for Industrial Applications, *J. Therm. Spray Technol.*, 2006, **15**(2), p 223-232

14. H. Assadi, T. Schmidt, H. Richter, J.-O. Kliemann, K. Binder, F. Gärtner, T. Klassen, and H. Kreye, On Parameter Selection in Cold Spraying, *J. Therm. Spray Technol.*, 2011, **20**(6), p 1161-1176

15. D.M. Chun, J.O. Choi, C.S. Lee, and S.H. Ahn, Effect of Stand-off Distance for Cold Gas Spraying of Fine Ceramic Particles under Low Vacuum and Room Temperature Using Nano-Particle Deposition System (NPDS), *Surf. Coat. Technol.*, 2012, **206**(8–9), p 2125-2132

16. W.Y. Li, C. Zhang, X.P. Guo, G. Zhang, H.L. Liao, C.J. Li, and C. Coddet, Effect of Standoff Distance on Coating Deposition Characteristics in Cold Spraying, *Mater. Des.*, 2008, **29**(2), p 297-304

17. W.-Y. Li, H. Liao, G. Douchy, and C. Coddet, Optimal Design of a Cold Spray Nozzle by Numerical Analysis of Particle Velocity and Experimental Validation with 316L Stainless Steel Powder, *Mater. Des.*, 2007, **28**(7), p 2129-2137

18. Abaqus Analysis User's Manual, ABAQUS 6.13 HTML Documentation, Dassault Systèmes, 2013, n.d.

19. X. Suo, S. Yin, M.-P. Planche, T. Liu, and H. Liao, Strong Effect of Carrier Gas Species on Particle Velocity during Cold Spray Processes, *Surf. Coat. Technol.*, 2015, **268**, p 90-93

20. B. Vreman, B.J. Geurts, N.G. Deen, J.A.M. Kuipers, and J.G.M. Kuerten, Two- and Four-Way Coupled Euler-Lagrangian Large-Eddy Simulation of Turbulent Particle-Laden Channel Flow, *Flow Turbul. Combust.*, 2009, **82**(1), p 47-71

21. S. Yin, X.F. Wang, and W.Y. Li, Computational Analysis of the Effect of Nozzle Cross-Section Shape on Gas Flow and Particle Acceleration in Cold Spraying, *Surf. Coat. Technol.*, 2011, **205**(8–9), p 2970-2977

22. S. Yin, M. Meyer, W. Li, H. Liao, and R. Lupoi, Gas Flow, Particle Acceleration, and Heat Transfer in Cold Spray: A Review, *J. Therm. Spray Technol.*, 2016, **25**(5), p 874-896

23. F.F. Wang, W.Y. Li, M. Yu, and H.L. Liao, Prediction of Critical Velocity during Cold Spraying Based on a Coupled Thermomechanical Eulerian Model, *J. Therm. Spray Technol.*, 2014, **23**(1–2), p 60-67

24. W.Y. Li, K. Yang, S. Yin, and X.P. Guo, Numerical Analysis of Cold Spray Particles Impacting Behavior by the Eulerian Method: A Review, *J. Therm. Spray Technol.*, 2016, **25**(8), p 1441-1460

25. W. Li, K. Yang, D. Zhang, and X. Zhou, Residual Stress Analysis of Cold-Sprayed Copper Coatings by Numerical Simulation, *J. Therm. Spray Technol.*, 2016, **25**(1–2), p 131-142

26. K. Yang, W. Li, X. Guo, X. Yang, and Y. Xu, Characterizations and Anisotropy of Cold-Spraying Additive-Manufactured Copper Bulk, *J. Mater. Sci. Technol.*, 2018, **34**(9), p 1570-1579

27. W. Li, K. Yang, D. Zhang, X. Zhou, and X. Guo, Interface Behavior of Particles upon Impacting during Cold Spraying of Cu/Ni/Al Mixture, *Mater. Des.*, 2016, **95**, p 237-246

28. M. Yu, W.Y. Li, F.F. Wang, and H.L. Liao, Finite Element Simulation of Impacting Behavior of Particles in Cold Spraying by Eulerian Approach, *J. Therm. Spray Technol.*, 2012, **21**(3), p 745-752

29. W.-Y. Li and W. Gao, Some Aspects on 3D Numerical Modeling of High Velocity Impact of Particles in Cold Spraying by Explicit Finite Element Analysis, *Appl. Surf. Sci.*, 2009, **255**(18), p 7878-7892

30. S. Yin, X. Wang, W. Li, H. Liao, and H. Jie, Deformation Behavior of the Oxide Film on the Surface of Cold Sprayed Powder Particle, *Appl. Surf. Sci.*, 2012, **259**, p 294-300

31. C. Zhang, Q. Chen, J. Liu, W. Tang, K. Wang, and J. Song, Numerical Study on the Effect of the Cold Powder Carrier Gas on Powder Stream Characteristics in Cold Spray, *Surf. Coat. Technol.*, 2016, **294**, p 177-185

32. C. Li, N. Singh, A. Andrews, B.A. Olson, T.E. Schwartzentruber, and C.J. Hogan, Mass, Momentum, and Energy Transfer in Supersonic Aerosol Deposition Processes, *Int. J. Heat Mass Transf.*, 2019, **129**, p 1161-1171

33. J. Pattison, S. Celotto, A. Khan, and W. O'neill, Standoff Distance and Bow Shock Phenomena in the Cold Spray Process, *Surface Coat. Technol.*, 2008, **202**(8), p 1443-1454

34. L. de Juan and J. Fernández de la Mora, Sizing Nanoparticles with a Focusing Impactor: Effect of the Collector Size, *J. Aerosol Sci.*, 1998, **29**(5), p 589-599

35. X. Wang, F.E. Kruis, and P.H. McMurry, Aerodynamic Focusing of Nanoparticles: I. Guidelines for Designing Aerodynamic Lenses for Nanoparticles, *Aerosol Sci. Technol.*, 2005, **39**(7), p 611-623

36. T. Schmidt, F. Gärtner, H. Assadi, and H. Kreye, Development of a Generalized Parameter Window for Cold Spray Deposition, *Acta Mater.*, 2006, **54**(3), p 729-742

37. J. Vlcek, L. Gimeno, H. Huber, and E. Lugscheider, A Systematic Approach to Material Eligibility for the Cold-Spray Process, *J. Therm. Spray Technol.*, 2005, **14**(1), p 125-133

38. D.-W. Lee, O.-Y. Kwon, W.-J. Cho, J.-K. Song, and Y.-N. Kim, Characteristics and Mechanism of Cu Films Fabricated at Room Temperature by Aerosol Deposition, *Nanoscale Res. Lett.*, 2016, **11**, p 162

39. X.-T. Luo, C.-X. Li, F.-L. Shang, G.-J. Yang, Y.-Y. Wang, and C.-J. Li, High Velocity Impact Induced Microstructure Evolution during Deposition of Cold Spray Coatings: A Review, *Surf. Coat. Technol.*, 2014, **254**, p 11-20